JGR Solid Earth

RESEARCH ARTICLE
10.1029/2021JB022233

Fluid Pressure Diffusion in Fractured Media: The Role Played by the Geometry of Real Fractures

Simón Lissa[1], Nicolás D. Barbosa[1], and Beatriz Quintal[1]

[1]Institute of Earth Sciences, University of Lausanne, Lausanne, Switzerland

Key Points:

- The anisotropic velocity of *P* and *S* waves traveling across real fractures can be reproduced using a planar-thin-layer model
- The attenuation of *S* waves is highly affected by a squirt-type flow prevailing inside fractures with mild curvature
- Our observations can help improve the interpretation and inversion of mechanical and hydraulic properties of fractures from seismic data

Supporting Information:

Supporting Information may be found in the online version of this article.

Correspondence to:

S. Lissa,
simon.lissa@unil.ch

Citation:

Lissa, S., Barbosa, N. D., & Quintal, B. (2021). Fluid pressure diffusion in fractured media: The role played by the geometry of real fractures. *Journal of Geophysical Research: Solid Earth*, *126*, e2021JB022233. https://doi.org/10.1029/2021JB022233

Received 13 APR 2021
Accepted 15 SEP 2021

Abstract Wave-induced fluid pressure diffusion (FPD) represents an important mechanism of seismic energy dissipation in fractured media. The associated effects on wave propagation are typically studied considering idealized fracture geometries. Here, we study fracture-geometry-related effects on FPD by numerically computing the frequency-dependent and angle-dependent seismic velocity and attenuation on models having fractures of realistic geometries. The geometry of the models is derived from microcomputed tomography images of a fractured Berea sandstone. By comparing the numerical results with those for an equivalent thin-planar-layer analytical model, we isolate fracture-geometry effects. We found that discrepancies on the anisotropic behavior of *P* and *S* waves with respect to the simple analytical model are small except for the *S* wave attenuation. This is associated with the pressure gradients induced by *S* waves in fractures exhibiting a mild curvature. Part of this dissipation occurs inside the fracture, parallel to its walls, and is thus controlled by its permeability, which points to a possible perspective of inferring fracture hydraulic properties from *S* waves attenuation.

Plain Language Summary The attenuation and velocity dispersion of seismic waves propagating in rocks can be used to infer and to characterize rock heterogeneities and fluid content. Fluid pressure diffusion is an important cause of such attenuation and dispersion and can be estimated using analytical and numerical solutions based on simple representations of fractures. A broadly used approach is to represent fractures as thin-planar poroelastic layers. However, the effects of complex fracture geometry, such as rough and curved walls and contact areas, remain largely unexplored. In this study, we numerically calculate the seismic energy dissipation due to fluid pressure diffusion in a medium containing a fracture of realistic geometry. We compare these results with those of a thin-planar layer to study the limitations of the simple model. We show that the *S* wave response for normal incidence can be strongly attenuated in part due to fluid pressure diffusion occurring inside the fracture and parallel to its walls triggered by a mild fracture curvature. Such effect cannot be accounted for by a thin-planar model. This points to the potential of estimating hydraulic fracture properties from the *S* wave attenuation.

1. Introduction

The presence of fractures modifies the mechanical and hydraulic properties of rocks, which can impact several activities from monitoring CO_2 geological sequestration and underground radioactive-waste repositories to geothermal energy and hydrocarbon production (e.g., Bakulin et al., 2000; Klimentos, 1995; Metz et al., 2005; Tester et al., 2007). Seismic methods represent a popular tool to detect and characterize fractures because seismic wave propagation can be strongly affected by their presence. In particular, an important physical mechanism for seismic attenuation and velocity dispersion occurs when a passing wave deforms a fluid-saturated fractured medium. The compressibility contrast between the compliant fractures and the stiffer embedding background allows for the generation of fluid pressure gradients between them. Then, seismic energy is dissipated due to viscous friction in the pore fluid during the associated fluid pressure diffusion (FPD) process (Pride et al., 2004; White et al., 1975). The frequency dependence of this process in fractured media has been theoretically studied either assuming idealized geometries such as, e.g., ellipsoids (Chapman, 2003; Masson & Pride, 2007, 2014), planar layers of either infinitely small (e.g., Brajanovski et al., 2005) or finite aperture (e.g., Quintal et al., 2014), and other more intricate although still artificial fracture geometries (Lissa et al., 2019; Rubino et al., 2014). Idealized geometries have also been considered for experimental studies (Amalokwu et al., 2015, 2016; Maultzsch et al., 2003; Tillotson et al., 2014). While

idealized fracture geometries are useful for simplifying the study of the effects of FPD on seismic waves, the characteristics of this phenomenon for real fracture geometries remain to be evaluated.

Real fractures can exhibit roughness and curvature of their walls, contact areas, as well as the presence of some degree of occlusion, mineralization, or other alteration processes (e.g., Jaeger et al., 2007; Karpyn et al., 2007; Masson & Pride, 2015; Montemagno & Pyrak-Nolte, 1999; Nakagawa et al., 2019). Considering that they are not simply empty cavities, a generally accepted, conceptually simple, and physically intuitive description of fractures is an effective fluid-saturated poroelastic inclusion (Brajanovski et al., 2005; Masson & Pride, 2007; Pride et al., 2004; Quintal et al., 2014; Rubino et al., 2013). Poroelastic fractures are often represented as single planar layers (Brajanovski et al., 2005; Nakagawa & Schoenberg, 2007; Quintal et al., 2014; Schoenberg, 1980), or as distributions of thin-planar layers (Caspari et al., 2016, 2019; Guo et al., 2018; Hunziker et al., 2018). Few studies consider more complex fracture geometries and analyze their impact on the seismic response of fractures. Rubino et al. (2014) considered 2D planar fractures to analyze the impact of the geometrical and mechanical properties of contact area distributions on the overall seismic response. This study was later generalized by Lissa et al. (2019) for more realistic 3D planar-fracture models, showing that the anisotropic seismic response in the presence of fractures having complex aperture distributions can be reproduced by an equivalent thin-planar-layer model (ETLM). Nakagawa et al. (2013) experimentally measured seismic attenuation due to FPD in a saturated Berea sandstone having a single nearly horizontal fracture that could not be reproduced by an ETLM, which points to the need of better understanding the limitations of this simplification.

In this work, we numerically compute the effective anisotropic velocity and attenuation of *P* and *S* waves under fluid-saturated conditions of a medium having a fracture of realistic geometry. The methodology is described in Section 2. First, in Section 2.1, we describe the workflow followed to create the numerical models. To do so, we use microcomputed tomography images of a fractured Berea sandstone sample (Karpyn et al., 2016) to reproduce the complexity of a real fracture geometry. Then, in Section 2.2, we provided the mathematical formulation used for the numerical solution based on Biot's equations (Biot, 1941). Also, we describe the employed numerical approach to obtain the seismically-induced effects of FPD in the fractures and background due to the action of *P* and *S* waves. In Section 2.3, we describe the methodology to obtain the properties required for the analytical solution of a typically employed ETLM. For this, we use an inversion procedure to infer the mechanical properties and effective aperture of the ETLM using the numerically obtained normal-incidence *P* wave modulus dispersion and compliance of the model with the realistic fracture. In Section 3, we present fracture-geometry-related effects and the limitations of the ETLM to reproduce the seismic response of a real fracture. Finally, in Section 4, we explain the impact of a real fracture geometry on FPD effects and illustrate the sensitivity of these effects to the fracture permeability.

2. Methodology

2.1. Fracture Models

We consider a cm-scale Berea sandstone sample containing an artificially created fracture following the procedure described by Karpyn et al. (2007). Here, we use the segmented image of the fracture (Karpyn et al., 2016), which was digitized in a way that it is split into four smaller fracture images of an approximately square shape of 22 mm per side. For the analysis, we consider them as independent fractures, each one embedded in a cubic background (Figure 1). To create the numerical models, we employ the software AVIZO 2019.1 (Thermo Fisher Scientific Inc.) for importing the segmented images, creating the cubic background embedding the fractures and generating a mesh only on the surfaces of both the fracture and the background.

Quintal et al. (2016) showed that seismic effects associated with FPD occurring inside planar fractures represented as a poroelastic medium exhibits similar behaviour as those obtained when fractures are modelled as cavities filled with a fluid in which linearized Navier-Stokes equations are solved. In this work, fractured are modelled as poroelastic inclusions having both contact areas and open spaces. This representation is based on the fact that real fractures can have some degree of occlusion, mineralization, or other alteration processes (e.g., Jaeger et al., 2007). The contact areas are assigned with the same bulk properties used for the background, which has properties representative of a Berea sandstone (Nakagawa & Schoenberg, 2007).

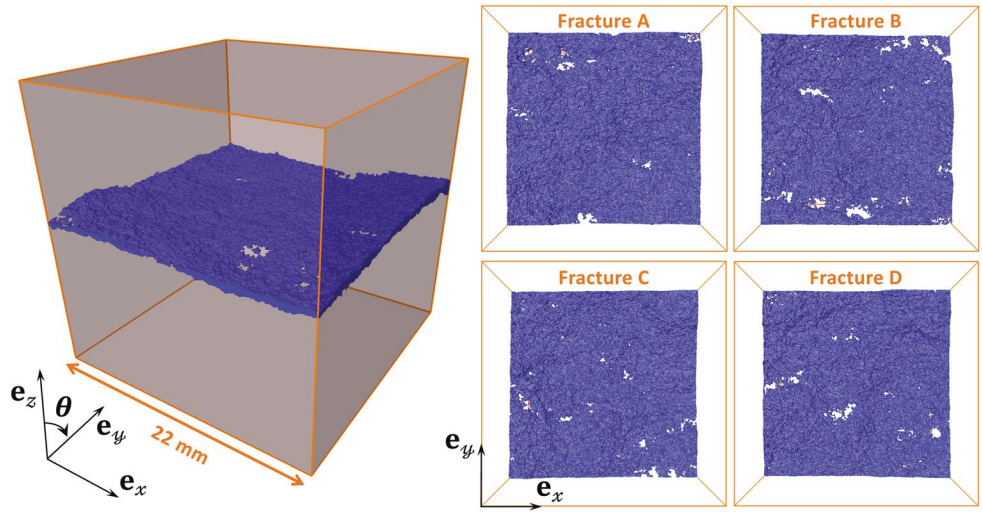

Figure 1. (left) Numerical model consisting of a cube (orange box) having ~22 mm per side and a fracture (blue region) in the middle. (right) Four different models are obtained by embedding each of the four fractures in such a cubic background.

For the open regions, we assume a solid matrix with high compressibility, porosity, and permeability to emulate fluid-filled open regions in a poroelastic context (Quintal et al., 2019). Given that FPD effects are largely dependent on the mechanical contrast between the fractures and the embedding background, we estimate the poroelastic fracture properties that minimize the difference on the overall deformation of the medium under dry conditions between models where fractures are represented as voids and as poroelastic inclusions (Supporting Information S1). Finally, at the grain level, same properties are used for the fractures and background. All material properties are listed in Table 1.

2.2. Numerical Framework

2.2.1. Equations of Poroelasticity

The seismic response of a fractured Berea sandstone is numerically modeled considering a poroelastic upscaling approach (Lissa et al., 2019; Masson & Pride, 2007; Quintal et al., 2011). For that, we solve the quasi-static Biot's equations (Biot, 1941) in the frequency domain, which are

$$\nabla \cdot \boldsymbol{\sigma} = 0, \tag{1}$$

$$i\omega \mathbf{w} = -\left(\frac{\kappa}{\eta}\right)\nabla p, \tag{2}$$

where $\boldsymbol{\sigma}$ is the total stress tensor, $\mathbf{w}$ is the relative fluid displacement vector, p is the fluid pressure, ω is the angular frequency and i is the complex unity. The material properties κ and η are the permeability and the fluid viscosity, respectively. These equations are coupled through

$$\boldsymbol{\sigma} = 2\mu_m \epsilon + \mathbf{I}\left(\lambda_m e - \alpha p\right), \tag{3}$$

$$p = -M\alpha e - M\nabla \cdot \mathbf{w}, \tag{4}$$

where ϵ is the strain tensor, $\mathbf{I}$ is the identity tensor, and e is the trace of the strain tensor. The symbols λ_m and μ_m are Lamé's parameters of the dry frame, and α and M are Biot's poroelastic parameters given by

$$\alpha = 1 - \frac{K_m}{K_s}, \tag{5}$$

Table 1
Material Properties for the Poroelastic Equations Used for Forward Modeling

	Background	Open regions of fractures
Grain bulk modulus	$K_s = 36$ GPa	$K_s = 36$ GPa
Grain density	$\rho_s = 2{,}700$ kg/m^3	$\rho_s = 2{,}700$ kg/m^3
Porosity	$\phi = 0.18$	$\phi = 0.9$
Permeability	$\kappa = 200$ mD	$\kappa = 10^5$ mD
Drained bulk modulus	$K_m = 9$ GPa	$K_m = 0.001$ GPa
Drained rock shear modulus	$\mu_m = 7$ GPa	$\mu_m = 0.001$ GPa
Fluid bulk modulus	$K_f = 2.25$ GPa	$K_f = 2.25$ GPa
Fluid density	$\rho_f = 1{,}000$ kg/m^3	$\rho_f = 1{,}000$ kg/m^3
Fluid viscosity	$\eta = 0.001$ Pa s	$\eta = 0.001$ Pa s

$$M = \left(\frac{\alpha - \phi}{K_s} + \frac{\phi}{K_f} \right)^{-1}, \tag{6}$$

where K_m, K_s, and K_f are the bulk modulus of the dry frame, of the grains, and of the fluid, respectively, and ϕ is the porosity.

Combining Equations 2 and 4, the following expression can be obtained:

$$\nabla \cdot \left(-\frac{\kappa}{\eta} \nabla p \right) + \alpha i\omega \nabla \cdot \mathbf{u} + \frac{i\omega p}{M} = 0, \tag{7}$$

where $\mathbf{u}$ is the solid displacement vector.

Equations 1 and 7 are so-called the $\mathbf{u}$-p formulation of Biot's equations (Biot, 1941). The weak form is derived considering that the gradient of fluid pressure is zero at the boundary of the spatial domain, thus a natural undrained boundary is inherent to our numerical solution (Appendix B of Quintal et al. (2011)) and does not need to be explicitly implemented. We use the commercial software COMSOL Multiphysics (i) to generate the volumetric mesh with tetrahedral elements of the fracture models described in Section 2.1 (Supporting Information S1) and (ii) to solve the weak form of Equations 1 and 7 following the finite element method.

2.2.2. Upscaling

Under the assumption that incident wavelengths are much larger than the size of the heterogeneities of a given medium, the effective seismic properties can be inferred from the spatially averaged stress and strain resulting from the application of either oscillatory stress (creep test) or displacement (relaxation test) fields on the boundaries of a representative elementary volume (REV) of the medium (Milani et al., 2016). In this work, we consider relaxation tests in which either a compressional or a shear oscillatory harmonic displacements is applied on one boundary of a cubic model. In the case of the compressional tests, we set to zero the displacements perpendicular to all the boundaries except for that where the harmonic displacement is applied. In the case of the shear tests, we apply a harmonic tangential displacement on one boundary of the model. On the opposite boundary, we set to zero all solid displacement components. On the lateral boundaries, those components of the solid displacement that are perpendicular to the applied displacement are set to zero. In both types of tests, no fluid flow is allowed to occur on any boundary of the model (i.e., undrained conditions). Due to the employed boundary conditions in our relaxation tests, the upscaled properties are representative of a medium consisting on a periodic repetition of the cubic numerical model (Figure 1). That is, a medium containing a periodic repetition in the vertical z-direction of semihorizontal fractures having infinite length in the x-direction and y-direction. In addition, the applied boundary conditions account for the strain and stress field interactions of consecutive fractures (Lissa et al., 2019; Milani et al., 2016). The mathematical description of the applied boundary conditions is given in Appendix A.

To obtain the full anisotropic response of the 3D Berea sandstone fractured model, we extend to 3D the procedure presented by Rubino et al. (2016) for 2D samples to compute the effective stiffness matrix ($\mathbf{C} \equiv C_{ij}$), which is also detailed in Jian et al. (2021). The complete anisotropic stiffness matrix requires subjecting the numerical model to three compressional and three shear tests applied in the three cartesian directions. Then, we compute for each test and frequency the spatially averaged stress σ_{ij} and strains ϵ_{ij} for $i, j = 1, 2, 3, 4, 5, 6$. Under the assumption that these quantities are related through an effective stiffness matrix, we follow a least-square minimization procedure to calculate, at each considered frequency, up to 21 independent C_{ij} coefficients. Then, we calculate the complex wave numbers ($\tilde{k}$) solving the dynamic plane wave equations using the components of the equivalent frequency-dependent complex-valued stiffness matrix (Rubino et al., 2016). Finally, using the complex velocities derived from the complex wave numbers ($\widetilde{V}_j(\omega, \theta) = \omega / \tilde{k}$), the velocities for the P, S_V, and S_H waves and the corresponding quality factors as function of the incident angle are calculated (Carcione, 2007) as

$$Q_j^{-1}(\omega, \theta) = -\frac{Im\widetilde{V}_j(\omega, \theta)^2}{Re\widetilde{V}_j(\omega, \theta)^2}, \tag{8}$$

$$V_j(\omega,\theta) = \left[\mathrm{Re}\left(\frac{1}{\widetilde{V}_j(\omega,\theta)}\right)\right]^{-1}, \tag{9}$$

where j represents the P-, S_V- or S_H-wave mode.

2.3. Equivalent Thin-Planar-Layer Model (ETLM)

To study the effects of the realistic geometry of the analyzed 3D numerical models, we compare their response with a broadly used analytical solution based on the thin-planar layer model (White et al., 1975), which can be used for a medium consisting of a periodic alternation of background layers and planar fractures. This analytical solution corresponds to a model with vertical (i.e., z-direction in Figure 1) transverse isotropy (VTI). First, we follow an inversion procedure to estimate the parameters of the analytical solution for the ETLM by adjusting the numerical results of the realistic models at normal incidence. Then, to obtain the response of the ETLM across all incidence angles, we use those estimated equivalent parameters in the analytical solution of Krzikalla and Müller (2011) for a 3D poroelastic VTI model consisting of a periodic repetition of a compliant planar-thin-layer (representing fractures) and a stiffer and thicker layer (representing the background). For that, we compute first the elements of the anisotropic stiffness matrix, and then the P and S wave velocities and attenuation as functions of frequency and incidence angle.

To make the simpler model (or ETLM) equivalent to our numerical model, which is based on a real fracture geometry, we systematically choose its properties. First, for the background, we use the same properties as for the numerical solution (Table 1). Second, the properties of the fracture in the ETLM need to be properly inferred to account for geometrical aspects of the real fracture such as roughness, distribution of contact areas, and curvature of the fracture walls, which affect the effective compliance, porosity, permeability, and aperture of the fracture. We follow a minimization procedure to obtain the equivalent aperture (h^{fr}_{eqv}) as well as dry bulk (K^{fr}_{eqv}) and shear (μ^{fr}_{eqv}) moduli for the planar layer. To do so, we minimize the discrepancies between the following properties obtained for the numerical model and for the ETLM: (a) the inverse of the dry normal and shear compliances and (b) the real component of the frequency-dependent effective P wave modulus at normal incidence (C_{33}). For (a), the dry normal and shear compliances for the numerical models are computed following Lissa et al. (2019) (Supporting Information S1), and for the ETLM predicted by using the analytical solution as

$$Z_N = f_c \,/\, C_{33}, \tag{10}$$

$$Z_T = f_c \,/\, C_{44}, \tag{11}$$

with $f_c = h_{fr}/L_z$, where h_{fr} is an effective fracture aperture and L_z is the model length. And for (b), the C_{33} for the numerical models is computed following the described upscaling methodology and for the ETLM as

$$\frac{1}{C(\omega)^{sat}_{33}} = \langle P_u^{-1}\rangle + \frac{2}{L_z(i\omega\eta)^{0.5}} \frac{((\alpha^b M^b \,/\, P^b_u) - (\alpha^{fr} M^{fr} \,/\, P^{fr}_u))^2}{\left(\frac{N^b}{\kappa^b}\right)^{0.5} cot\left([1+i]k^b \frac{L-h^{fr}}{2}\right) + \left(\frac{N^{fr}}{\kappa^{fr}}\right)^{0.5} cot\left([1+i]k^{fr}\frac{h^{fr}}{2}\right)}, \tag{12}$$

where $k^j = (\omega\eta \,/\, 2\kappa^j N^j)^{0.5}$ with $j = b, fr$ being the properties of the background and fracture, respectively. P_d and P_u are the drained and undrained P wave moduli, respectively, and $N = M\frac{P_d}{P_u}$.

For the minimization, we use the package fminsearchcon developed for MATLAB (D'Errico, 2006), which finds the minimum of a constrained multivariable function using the derivative-free method. We define the vector

$$\mathbf{f} = \left[C(\omega_1)^{nu}_{33} - C(\omega_1)^{an}_{33}, C(\omega_2)^{nu}_{33} - C(\omega_2)^{an}_{33}, \ldots, C(\omega_n)^{nu}_{33} - C(\omega_n)^{an}_{33}, \frac{1}{Z^{nu}_N} - \frac{1}{Z^{an}_N}, \frac{1}{Z^{nu}_T} - \frac{1}{Z^{an}_T}\right], \tag{13}$$

where nu and an correspond to the 3D realistic model numerically obtained and to the 1D analytical solution, respectively, and n corresponds to the number of evaluated frequencies (in this work, 7). Then, we minimize the square of norm 2 of the vector $\mathbf{f}$, i.e., $F = \| \mathbf{f} \|^2_2$. Assuming that the fracture permeability is much higher than that of the background, the fluid-pressure relaxation process is controlled by the

Table 2
Inverted Equivalent Properties of Each Real Fracture to be Used in the ETLM

Model	η_n (m / Pa)	η_t (m / Pa)	η_n / η_t	K_{eqv}^{fr} (GPa)	μ_{eqv}^{fr} (GPa)	h_{eqv}^{fr} (mm)
A	4.44×10^{-12}	7.07×10^{-12}	0.63	0.0220	0.0864	0.611
B	2×10^{-12}	3.28×10^{-12}	0.61	0.0462	0.1516	0.498
C	2.83×10^{-12}	5.14×10^{-12}	0.551	0.0484	0.1007	0.519
D	3.17×10^{-12}	5.34×10^{-12}	0.593	0.0378	0.1097	0.587

background permeability (Barbosa et al., 2020). Therefore, we set the fracture permeability of the planar layer to that of the open regions of the fracture in the numerical model, which is arbitrarily chosen to be much higher than that of the background. The same is done for the porosity and, thus, we let the equivalent planar-layer aperture (h_{eqv}^{fr}) accommodate the effective pore fluid storage of the real fracture. Due to the geometrical differences between the real and planar fractures, the effective porosity of both models can differ. The convergence of the final values during the inversion procedure is verified by considering multiple initial values of parameters to be optimized ($h_{eqv}^{fr}, K_{eqv}^{fr}$, and μ_{eqv}^{fr}). As a result of all those cases, we obtain the same final values for the optimized parameters. The material properties finally used for the planar fracture in the analytical solution are given in Table 1 and the optimized parameters (h_{eqv}^{fr}, K_{eqv}^{fr}, and μ_{eqv}^{fr}) are given in Table 2.

3. Results and Discussion

In this section, we compare the seismic responses of the fractures having realistic geometries (Figure 1) with those of the ETLM. We first analyze the case of *P* waves with normal incidence and then we extend the analysis to *P* and *S* waves with oblique incidence.

3.1. *P* Wave Velocity Dispersion and Attenuation for Normal Incidence

Figure 2 shows the numerically computed *P* wave velocity dispersion and attenuation for the four fracture models shown in Figure 1. The imposed solid deformation on the top boundary of the numerical model generates a heterogeneous fluid pressure distribution, which depends on the geometrical, mechanical, and hydraulic characteristics of the fracture as well as on the frequency of the imposed oscillation. When the elapsed time during half wave period is similar to the time required for FPD to occur, energy is dissipated (Müller et al., 2010; Pride, 2005). For the chosen material and geometrical properties, attenuation and dispersion are mainly associated with FPD between the fracture and the embedding background and they are maximal at 10^4 Hz (Figure 2). At the highest considered frequency, the time elapsed during half wave period is not long enough to allow significant FPD. At this frequency, attenuation is lower than at 10^4 Hz and the *P* wave velocity is highest due to the maximum stiffening effect of the fluid in the pores. Moreover, the reduction of the attenuation and the flattening of the velocities with increasing frequency indicate the tendency

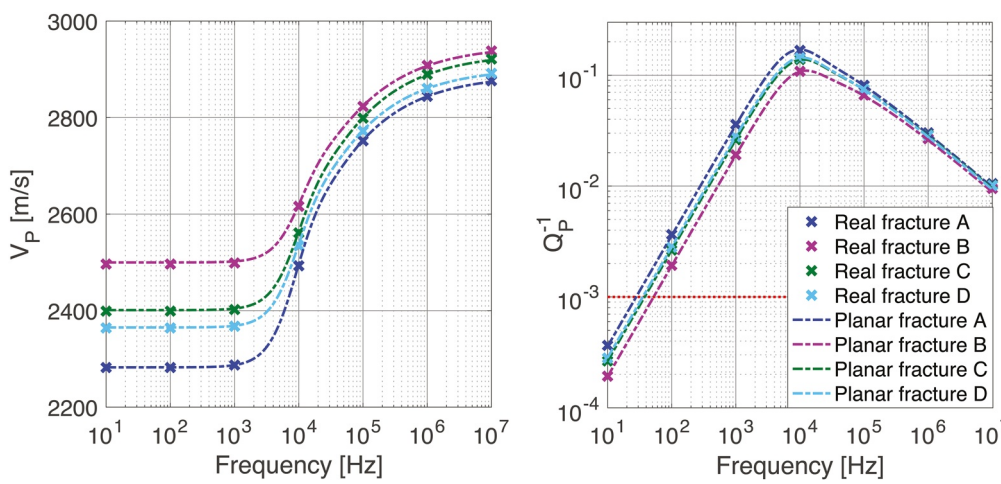

Figure 2. *P* wave velocity (V_P) and attenuation (Q_P^{-1}) for normal incidence as functions of frequency. Crosses correspond to the numerical solutions for each model based on a real fracture geometry and dashed lines denote the corresponding analytical solutions for each equivalent thin-planar-layer model (ETLM) (Table 2).

of the curves to reach the high frequency limit, or unrelaxed state, at which no FPD occurs. At the low-frequency limit, half wave period provides enough time for the fluid pressure gradients to fully equilibrate thus, minimizing the pore fluid stiffening effect on the *P* wave velocity, and attenuation is negligible. This scenario is commonly referred to as the relaxed frequency limit. Although the considered fracture models are subsamples of the same fracture, differences up to ~ 10% (at the lowest frequencies) between their *P* wave velocities can be observed. This already points to the important role played by the geometries of the fractures. However, the characteristic frequency (at which attenuation is maximal), which depends mainly on the background permeability, thicknesses of the background, and relative aperture (or volume fraction) of the fracture (Carcione et al., 2013), remains the same for all the models. Table 2 shows the equivalent apertures for the four models with variations of up to ~ 20%.

Figure 2 also shows the *P* wave velocity and attenuation obtained with the analytical solution for the planar fracture with the equivalent elastic moduli K_{eqv}^{fr} and μ_{eqv}^{fr} and aperture h_{eqv}^{fr} of the four ETLM given in Table 2. The effective fracture compliances (η_n, η_t) can be obtained from the compliances treated in this manuscript as $\eta_n = L_z Z_N$ and $\eta_t = L_z Z_T$. These values ($\eta_n \sim 10^{-12}$[mPa^{-1}]) are in the order of expected values for the scales of the models (mm to cm), as reviewed by Barbosa et al. (2019). The fracture compliance ratio (i.e., η_n / η_t) are close to those found by Nakagawa et al. (2013) (~0.55) from laboratory measurements on a fractured Berea sandstone sample. Moreover, the excellent agreement observed between the numerical and analytical solutions not only validates our optimization approach of fracture properties but, more importantly, it indicates that an ETLM can reproduce the *P* wave velocity for normal incidence for a fracture of realistic geometry having a mild curvature. In the following, we explore this comparison for other incidence angles of *P* waves as well as *S* waves.

3.2. *P* and *S* Wave Velocities and Attenuation as Functions of Frequency and Incident Angle

In this section, we only consider results for the fracture model A of Figure 1, which is the fracture exhibiting the highest velocity dispersion and attenuation due to FPD between the background and the fracture. We analyze the response of the *P* and the *S* waves, in the following subsections, for both, the numerical realistic models and the ETLM following the analytical solution of Krzikalla and Müller (2011).

3.2.1. *P* Wave

Figure 3 shows the *P* wave velocity dispersion (a) and attenuation (b) as functions of the incident angle (θ) at the relaxed limit, unrelaxed limit, and at intermediate frequencies for the model with a real fracture and the ETLM with VTI (Krzikalla & Müller, 2011). Figures 3a and 3b show that the maximum discrepancy between the *P* wave velocities is found at intermediate angles ($\theta \sim [30° - 60°]$) and it is always lower than 1%. Discrepancies can be observed for the attenuation curves at $\theta \sim [60° - 90°]$ at 10^5 and 10^7 Hz, although they are significant only when values are close or below to an estimated minimum attenuation magnitude that can be measured in laboratory experiments (e.g., Borgomano et al., 2020; Spencer & Shine, 2016). We denote the minimum observable attenuation with a red dotted line in the attenuation plots of Figures 2–4 at $Q^{-1} = 10^{-3}$. Figure 3 also shows the *P* wave velocity dispersion (c) and attenuation (d) as functions of frequency. Note that the excellent fitting for normal incidence ($\theta = 0°$ of Figures 3c and 3d) that was optimized with the inversion procedure is the same already shown in Figure 2 (blue curve). The minor discrepancies between the models can also be observed on the attenuation curves at $\theta = 60°$ and $\theta = 90°$ at frequencies higher than 10^5 Hz. This means that the relaxation process for the real fracture is slightly changing with the incidence angle, while it remains predominantely unidimensional for the ETLM as shown by Müller and Rothert (2006). Based on Figure 3, we can conclude that an ETLM can satisfactory reproduce the anisotropic seismic response of *P* waves, for incident angles lower than 30°, across a real fracture exhibiting low curvature, variable aperture, and contact areas. For higher incident angles, and at frequencies higher than 10^5 Hz moderate discrepancies can be observed in the attenuation curve. The physical process behind these observations will be discussed in Section 4.

3.2.2. *S* Wave

Now, we consider the two *S* wave modes coexisting in anisotropic media (Mavko et al., 2009). In this case, the S_V motion is contained in the plane *yz* for $\theta = 0°$ and for $\theta = 90°$ (Figure 1), while the S_H mode displacements occur in the plane *xz* for $\theta = 0°$ and in the plane *xy* for $\theta = 90°$. Figure 4 shows the *S* wave velocity

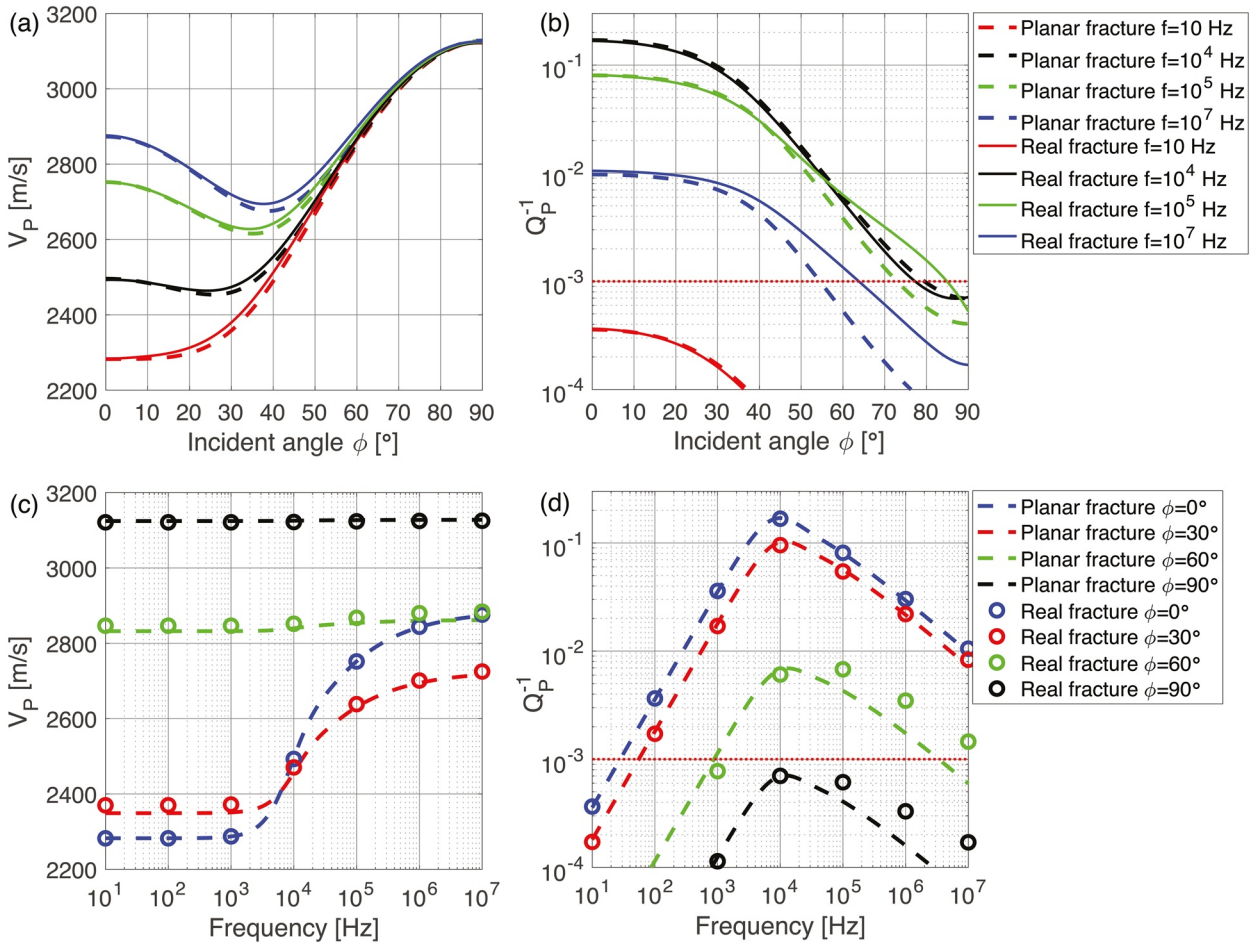

Figure 3. *P* wave velocity and attenuation as functions of the incident angle (a, b) and frequency (c, d), respectively, for model A based on the numerical solutions for fractures of real geometries (solid lines and circles) and the analytical solutions for the corresponding equivalent thin-planar-layer model (ETLM) (dashed lines).

dispersion (c) and attenuation (d) as functions of frequency for $\theta = 0°$ (normal incidence) and $\theta = 45°$ for both considered models. The complex response of the real fracture is accurately reproduced by the ETLM for the S_V wave at $\theta = 45°$. In that case, the characteristic frequency ($\sim 10^4$ Hz) matches that of the *P* wave velocity for normal incidence, as expected for an ETLM. However, unlike for *P* waves, normally incident *S* waves exhibit a different attenuation peak at $\sim 10^6$ Hz, which cannot be reproduced by an ETLM. The same occurs for S_H waves at $\theta = 45°$. Figure 4 also shows the *S* wave velocities (a) and attenuation (b) for both models at 10 Hz (relaxed limit) and at 10^6 Hz (characteristic frequency of the *S* waves at $\theta = 0°$). At 10^6 Hz, the S_V attenuation has a clear maximum around $\theta = 50°$ for the ETLM (Figure 4b). However, the real-fracture model exhibits significant attenuation at all incidence angles, which results in a remarkably isotropic behavior of the S_V wave. The S_H wave, on the other hand, also exhibits measurable attenuation in the real-fracture model (at $\theta \sim [0° - 70°]$) that cannot be accounted for by an ETLM, which predicts zero attenuation. For $\theta = 0°$ both *S* wave modes show similar attenuation magnitudes, which means that the fracture is fairly isotropic in the *xy*-plane. The S_H wave presents negligible attenuation for $\theta = 90°$ because the fracture deformation is minimal in the plane *xy*, containing the fracture. While the fitting of *S* wave velocities is as satisfactory as for *P* waves, we found that, unlike for *P* waves, the ETLM cannot accurately reproduce the anisotropic attenuation of *S* waves in the presence of a real fracture.

To further understand the physical mechanism behind the *S* wave attenuation we calculate the local attenuation in different regions (Solazzi et al., 2016) when the model is subjected to a shear test emulating the action of normally incident *S* waves. Figure 5a shows the *S* wave attenuation for model A saturated with

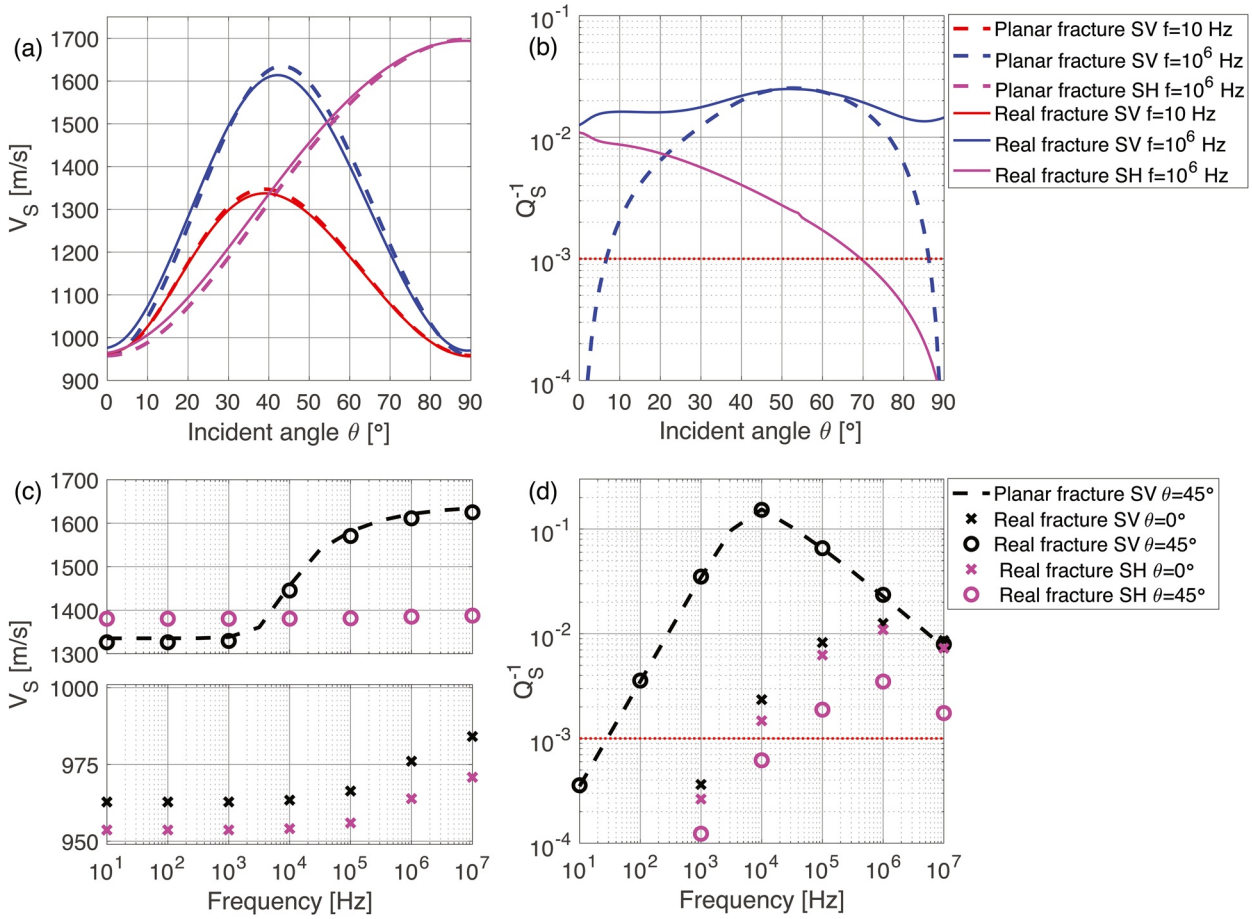

Figure 4. *S* wave velocity and attenuation as functions of the incident angle (a, b) and frequency (c, d), respectively, for model A based on the numerical solutions for fractures of real geometries (solid lines, crosses, and circles) and the analytical solutions for the corresponding equivalent thin-planar-layer model (ETLM) (dashed lines). Note that in panel (b), S_V wave attenuation at 10 Hz (red curves) and S_H wave attenuation for the ETLM (violet dashed curve) do not appear because they are negligible.

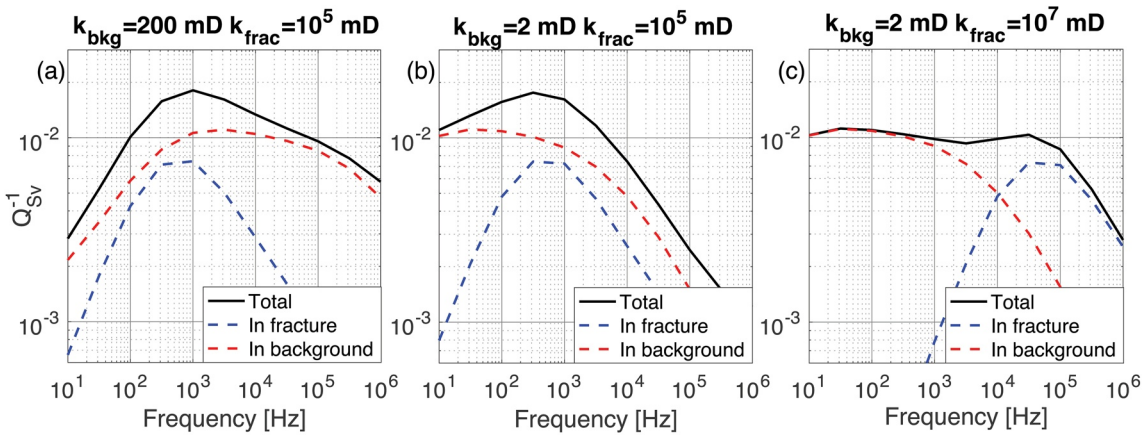

Figure 5. *S* wave attenuation at normal incidence ($\theta = 0°$) as function of frequency for the fractured model A considering different background (k_{bkg}) and fracture (k_{frac}) permeabilities. Black solid lines denote the total attenuation in the whole model. Red and blue dashed lines correspond to the attenuation taking place only in the background and only in the fracture, respectively.

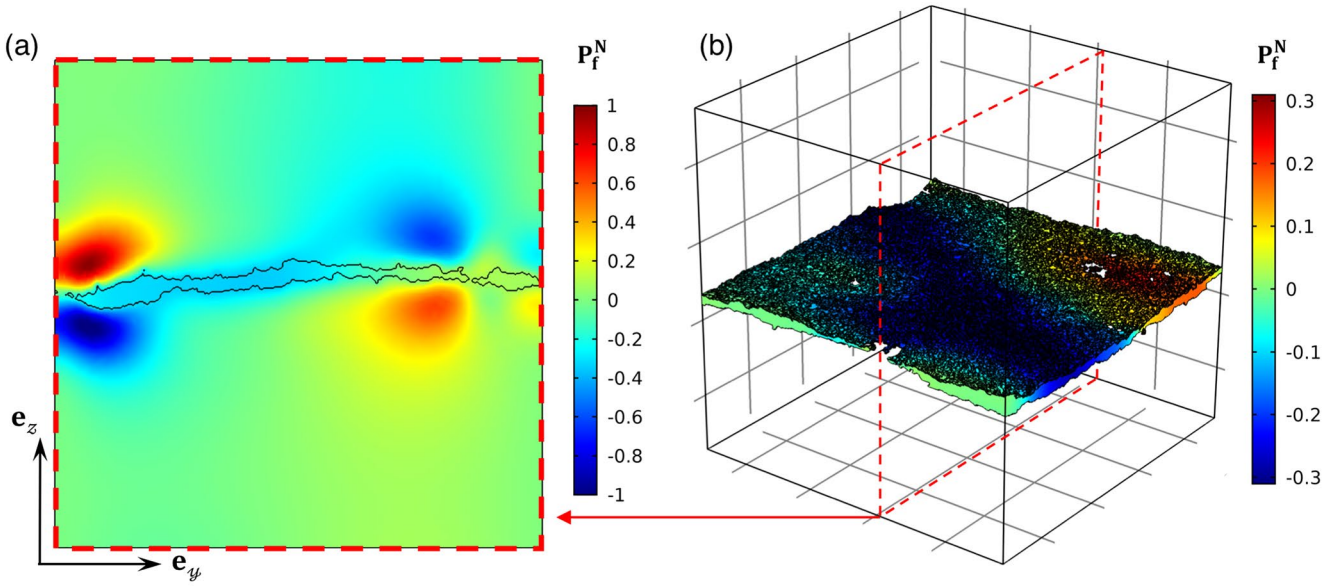

Figure 6. Normalized pore fluid pressure for a *S* wave at normal incidence for the permeabilities corresponding to Figure 5a on a slice perpendicular to the fracture (a) and inside the fracture (b) at 10^3 Hz.

glycerin ($K_f = 4.35$ GPa, $\mu_f = 0$ GPa, and $\eta_f = 1$ Pa s). We change the saturating fluid from water to glycerin, as commonly used in laboratory experiments (e.g., Borgomano et al., 2017, 2020; Pimienta et al., 2015; Subramaniyan et al., 2015), to shift the characteristic frequency previously observed at 10^6 Hz (Figure 4d) to 10^3 Hz (Figure 5a), thus keeping the attenuation curves inside the analyzed frequency range when changing the permeability in the models. We observe that both the dissipation in the fracture and in the background contribute to the total attenuation of a normally incident *S* wave. Again, for the ETLM, attenuation is negligible in both regions. To separate the frequency ranges at which effects occurring in the fracture and the background prevail, the background permeability is changed in Figure 5b. By doing so, the dissipation taking place in the background is significantly shifted to lower frequencies while the total attenuation is only slightly shifted. Figure 5c shows the effects of increasing fracture permeability while keeping it in the range of realistic magnitudes (Karpyn & Piri, 2007). In this case, the characteristic frequency of the attenuation taking place inside the fracture is shifted toward higher frequencies ($\sim 3 \times 10^4$ Hz), which, in turn, is manifested as a second attenuation peak on the total attenuation curve.

For the model depicted in Figure 5a, Figure 6a shows the normalized (with respect to the maximum) fluid pressure on a slice of the model perpendicular to the fracture, as a result of the same shear test at 10^3 Hz. The fluid pressure gradients observed in the background trigger the FPD responsible for the attenuation in the background (dashed red line) observed in Figure 5a. Likewise, Figure 6b shows the normalized fluid pressure inside the real fracture whose gradient gives rise to the FPD responsible for the attenuation inside the fracture (dashed blue line) shown in Figure 5a.

4. Squirt-Type Flow in a Real Fracture

Mild curvature of real fractures allows for a heterogeneous compression of the fracture and thus the generation of pressure gradients responsible for a squirt-type flow inside the fracture, in addition to the typical FPD between fractures and embedding background. Lissa et al. (2019) have shown that the seismic response of horizontal fractures with rough walls can be accurately reproduced by an ETLM having equivalent properties for all wave modes and incident angles. However, the middle plane of their fracture models were horizontal (i.e., not curved). Based on that, we conclude that the mild curvature of the fractures is responsible for the additional FPD effects observed in this contribution.

This squirt-type flow produces a contribution to the attenuation which is measurable based on current instrumental accuracy and that, as far as we know, has not been observed or quantified before. The squirt-type

flow or FPD taking place inside the fracture is mainly parallel to the fracture walls, which implies that it is sensitive to the fracture permeability. Such squirt-type flow inside fractures has been described by Rubino et al. (2013) and Quintal et al. (2014) in the case of seismic waves propagating across fractures that are hydraulically interconnected. In that case, FPD is also parallel to the fracture walls (Quintal et al., 2019) and controlled by the fracture permeability. Rubino et al. (2017) also found that associated effects can be more prominent for *S* waves than for *P* waves. In both scenarios, this is related to the different deformation caused by each wave mode. While the *P* wave either compresses or dilates during half wave cycle, the *S* wave induces both compression or extension depending on the orientation of the fractures in the model. As a result, the fluid pressure gradients induced by *S* waves can be much greater than those generated by *P* waves, and thus, attenuation. In the case of a single fracture, this relates to the curvature of the fracture while for multiple intersecting fractures it is often associated with the orientation of each individual fracture.

Nakagawa et al. (2013) performed laboratory experiments of oscillatory axial and shear (torsion) stresses applied normal to a nearly horizontal real fracture in a water-saturated Berea sandstone sample. FPD-related effects between the fracture and the background could be well explained using an ETLM for the compressional test. However, significant attenuation was also observed for the shear test, which could not be explained using an ETLM. According to our results, the attenuation for a normal-incident *S* wave due to FPD taking place not only in the background but also due to a squirt-type flow inside the fracture can be considered as a possible explanation for their observation.

In this study, we adopted a poroelastic representation for a fracture using Biot's equations as previously done in others works (Brajanovski et al., 2005; Lissa et al., 2019; Masson & Pride, 2007; Quintal et al., 2011; Rubino et al., 2013). However, different modeling schemes, such as the linearized Navier-Stokes equations (e.g., Quintal et al., 2019) can be used. While the existence of the squirt flow inside the fracture does not depend on the chosen modeling approach, its magnitude and frequency behavior can be highly affected by the way fractures are conceptualized. This is partly due to the different permeability distribution inside the fracture for each modeling approach. Implementation and comparison of different modeling schemes can be part of future work. In addition, we employed a constant and high permeability value for the open regions of the fracture, which is not linked to the aperture distribution. However, we showed that, by changing this permeability value, the frequency range of the attenuation occurring inside the fractures is shifted proportionally while the magnitude and frequency dependence of the attenuation remains unchanged.

5. Conclusions

We numerically calculated the effective seismic attenuation due to FPD associated with the presence of mesoscopic fractures on models derived from microcomputed tomography images of a fractured sample of Berea sandstone. We showed that an ETLM can fairly approximate the *P* wave velocity dispersion and attenuation for the models based on real fractures at all incidence angles.

We found that a mild curvature of a fracture causes a normally incident *S* wave to be significantly attenuated, which is in disagreement with the analytical solution for an ETLM. We showed that the FPD between the fracture and the background and, also, inside the single fracture and approximately parallel to its walls, are responsible for these effects. These effects are particularly relevant and observable when analyzing the anisotropy of *S* wave attenuation. Our results not only help to improve the understanding of the seismic response of real fractures but also points to the possible perspective of inferring other practically important parameters of fractured media, such as fracture permeability, from *S* wave attenuation.

Appendix A: Boundary Conditions

To calculate the effective *P* and *S* wave moduli of the considered models, we apply oscillatory harmonic test using the following boundary conditions. We define the domain of the model volume as $\Omega = L_x \times L_y \times L_z$ and its boundary $\Gamma = \Gamma^{L1} \cup \Gamma^{L2} \cup \Gamma^{L3} \cup \Gamma^{L4} \cup \Gamma^{T} \cup \Gamma^{B}$ where

$$\Gamma^{L1} = [(x, y, z) \in \Omega : x = 0], \tag{A1}$$

$$\Gamma^{L2} = [(x, y, z) \in \Omega : x = L_x], \tag{A2}$$

$$\Gamma^{L3} = [(x, y, z) \in \Omega : y = 0], \tag{A3}$$

$$\Gamma^{L4} = [(x, y, z) \in \Omega : y = L_y], \tag{A4}$$

$$\Gamma^{T} = [(x, y, z) \in \Omega : z = L_z], \tag{A5}$$

$$\Gamma^{B} = [(x, y, z) \in \Omega : z = 0]. \tag{A6}$$

We define $\mathbf{n}$, $\mathbf{t}_i$ and $\mathbf{t}_j$ as the unit normal and unit tangents vectors, respectively, to each boundary of Γ, with $i, j = x, y, z$ states for the orientation of the unit tangents and $i \perp j$. In the case of the compressional test parallel to the z-direction, we set the boundary conditions as

$$\mathbf{u} \cdot \mathbf{n} = -u^0, \text{on } \Gamma^{T}, \tag{A7}$$

$$\mathbf{u} \cdot \mathbf{n} = 0, \text{on } \Gamma^{L1} \cup \Gamma^{L2} \cup \Gamma^{L3} \cup \Gamma^{L4} \cup \Gamma^{B}, \tag{A8}$$

$$\left(\boldsymbol{\sigma}\mathbf{n}\right) \cdot \mathbf{t}_x = 0, \left(\boldsymbol{\sigma}\mathbf{n}\right) \cdot \mathbf{t}_y = 0, \text{on } \Gamma, \tag{A9}$$

$$\nabla p \cdot \mathbf{n} = 0, \text{on } \Gamma, \tag{A10}$$

In the case of a shear test applied in the xz-plane we set the boundary conditions as

$$\mathbf{u} \cdot \mathbf{t}_x = -u^0, \left(\boldsymbol{\sigma}\mathbf{n}\right) \cdot \mathbf{t}_y = 0, \left(\boldsymbol{\sigma}\mathbf{n}\right) \cdot \mathbf{t}_z = 0, \text{on } \Gamma^{T}, \tag{A11}$$

$$\left(\boldsymbol{\sigma}\mathbf{n}\right) \cdot \mathbf{t}_x = 0, \mathbf{u} \cdot \mathbf{t}_y = 0, \mathbf{u} \cdot \mathbf{t}_z = 0, \text{on } \Gamma^{L1} \cup \Gamma^{L2} \cup \Gamma^{L3} \cup \Gamma^{L4}, \tag{A12}$$

$$\mathbf{u} = \mathbf{0}, \text{on } \Gamma^{B}, \tag{A13}$$

$$\nabla p \cdot \mathbf{n} = 0, \text{on } \Gamma. \tag{A14}$$

Data Availability Statement

These data are available online (at http://doi.org/10.5281/zenodo.4683013).

Acknowledgments
This research has been supported by the Swiss National Science Foundation (Grant No. 172691). N. D. B. was partially supported by a SPARK grant from the SNF (Grant No. 196037). We acknowledge helpful comments from the editors and the reviewers. We also thank Klaus Holliger and Marco Favino for enlightening suggestions. Open access funding provided by Universite de Lausanne.

References

Amalokwu, K., Best, A. I., & Chapman, M. (2016). Effects of aligned fractures on the response of velocity and attenuation ratios to water saturation variation: A laboratory study using synthetic sandstones. *Geophysical Prospecting*, *64*(4), 942–957. https://doi.org/10.1111/1365-2478.12378

Amalokwu, K., Chapman, M., Best, A. I., Minshull, T. A., & Li, X.-Y. (2015). Water saturation effects on P-wave anisotropy in synthetic sandstone with aligned fractures. *Geophysical Journal International*, *202*(2), 1088–1095. https://doi.org/10.1093/gji/ggv192

Bakulin, A., Grechka, V., & Tsvankin, I. (2000). Estimation of fracture parameters from reflection seismic data—Part I: HTI model due to a single fracture set. *Geophysics*, *65*(6), 1788–1802. https://doi.org/10.1190/1.1444863

Barbosa, N. D., Caspari, E., Rubino, J. G., Greenwood, A., Baron, L., & Holliger, K. (2019). Estimation of fracture compliance from attenuation and velocity analysis of full-waveform sonic log data. *Journal of Geophysical Research: Solid Earth*, *124*, 2738–2761. https://doi.org/10.1029/2018JB016507

Barbosa, N. D., Kpke, C., Caspari, E., Rubino, J. G., Irving, J., & Holliger, K. (2020). Impact of poroelastic effects on the inversion of fracture properties from amplitude variation with offset and azimuth data in horizontal transversely isotropic media. *Geophysics*, *85*(5), N27–N39. https://doi.org/10.1190/geo2019-0475.1

Biot, M. A. (1941). General theory of three-dimensional consolidation. *Journal of Applied Physics*, *12*, 155–164. https://doi.org/10.1063/1.1712886

Borgomano, J. V. M., Gallagher, A., Sun, C., & Fortin, J. (2020). An apparatus to measure elastic dispersion and attenuation using hydrostatic- and axial-stress oscillations under undrained conditions. *Review of Scientific Instruments*, *91*(3), 034502. https://doi.org/10.1063/1.5136329

Borgomano, J. V. M., Pimienta, L., Fortin, J., & Guguen, Y. (2017). Dispersion and attenuation measurements of the elastic moduli of a dual-porosity limestone. *Journal of Geophysical Research: Solid Earth*, *122*, 2690–2711. https://doi.org/10.1002/2016JB013816

Brajanovski, M., Gurevich, B., & Schoenberg, M. (2005). A model for P-wave attenuation and dispersion in a porous medium permeated by aligned fractures. *Geophysical Journal International*, *163*(1), 372–384. https://doi.org/10.1111/j.1365-246X.2005.02722.x

Carcione, J. (2007). *Wave fields in real media: Wave propagation in anisotropic, anelastic, porous and electromagnetic media*. Amsterdam: Elsevier.

Carcione, J., Gurevich, B., Santos, J., & Picotti, S. (2013). Angular and frequency-dependent wave velocity and attenuation in fractured porous media. *Pure and Applied Geophysics*, *170*, 1673–1683. https://doi.org/10.1007/s00024-012-0636-8

Caspari, E., Milani, M., Rubino, J. G., Müller, T. M., Quintal, B., & Holliger, K. (2016). Numerical upscaling of frequency-dependent P- and S-wave moduli in fractured porous media. *Geophysical Prospecting*, *64*(4), 1166–1179. https://doi.org/10.1111/1365-2478.12393

Caspari, E., Novikov, M., Lisitsa, V., Barbosa, N. D., Quintal, B., Rubino, J. G., & Holliger, K. (2019). Attenuation mechanisms in fractured fluid-saturated porous rocks: A numerical modelling study. *Geophysical Prospecting*, *67*(4), 935–955. https://doi.org/10.1111/1365-2478.12667

Chapman, M. (2003). Frequency-dependent anisotropy due to meso-scale fractures in the presence of equant porosity. *Geophysical Prospecting*, *51*, 369–379. https://doi.org/10.1046/j.1365-2478.2003.00384.x

D'Errico, J. (2006). Fminsearchbnd. MATLAB Central File Exchange. Retrieved from https://www.mathworks.com/matlabcentral/fileexchange/8277-fminsearchbnd-fminsearchcon

Guo, J., Rubino, J. G., Barbosa, N. D., Glubokovskikh, S., & Gurevich, B. (2018). Seismic dispersion and attenuation in saturated porous rocks with aligned fractures of finite thickness: Theory and numerical simulations—Part 1: P-wave perpendicular to the fracture plane. *Geophysics*, *83*(1), WA49–WA62. https://doi.org/10.1190/geo2017-0065.1

Hunziker, J., Favino, M., Caspari, E., Quintal, B., Rubino, J. G., Krause, R., & Holliger, K. (2018). Seismic attenuation and stiffness modulus dispersion in porous rocks containing stochastic fracture networks. *Journal of Geophysical Research: Solid Earth*, *123*, 125–143. https://doi.org/10.1002/2017JB014566

Jaeger, J., Cook, G. W. N., & Zimmerman, R. (2007). *Fundamental of rock mechanics*. Wiley-Blackwell. https://doi.org/10.1017/CBO9780511735349

Jian, S., Fu, L-Y., Cao, C., Han, T., & Du, Q. (2021). 3D finite-element modeling of effective elastic properties for fracture density and multiscale natural fractures. *Journal of Geophysics and Engineering*, *18*(4), 567–582. http://doi.org/10.1093/jge/gxab036

Karpyn, Z., Grader, A., & Halleck, P. (2007). Visualization of fluid occupancy in a rough fracture using micro-tomography. *Journal of Colloid and Interface Science*, *307*(1), 181–187. https://doi.org/10.1016/j.jcis.2006.10.082

Karpyn, Z., Landry, C., & Prodanovic, M. (2016). *Induced rough fracture in Berea sandstone core*. Digital Rocks Portal. Retrieved from http://www.digitalrocksportal.org/projects/31 https://doi.org/10.17612/P7J012

Karpyn, Z., & Piri, M. (2007). Prediction of fluid occupancy in fractures using network modeling and x-ray microtomography. I: Data conditioning and model description. *Physical Review E*, *76*, 016315. https://doi.org/10.1103/PhysRevE.76.016315

Klimentos, T. (1995). Attenuation of P- and S-waves as a method of distinguishing gas and condensate from oil and water. *Geophysics*, *60*(2), 447–458. https://doi.org/10.1190/1.1443782

Krzikalla, F., & Müller, T. M. (2011). Anisotropic P-SV-wave dispersion and attenuation due to inter-layer flow in thinly layered porous rocks. *Geophysics*, *76*(3), WA135–WA145. https://doi.org/10.1190/1.3555077

Lissa, S., Barbosa, N. D., Rubino, J. G., & Quintal, B. (2019). Seismic attenuation and dispersion in poroelastic media with fractures of variable aperture distributions. *Solid Earth*, *10*(4), 1321–1336. https://doi.org/10.5194/se-10-1321-2019

Masson, Y. J., & Pride, S. R. (2007). Poroelastic finite difference modeling of seismic attenuation and dispersion due to mesoscopic-scale heterogeneity. *Journal of Geophysical Research*, *112*, B03204. https://doi.org/10.1029/2006JB004592

Masson, Y. J., & Pride, S. R. (2014). On the correlation between material structure and seismic attenuation anisotropy in porous media. *Journal of Geophysical Research: Solid Earth*, *119*, 2848–2870. https://doi.org/10.1002/2013JB010798

Masson, Y. J., & Pride, S. R. (2015). Mapping the mechanical properties of rocks using automated microindentation tests. *Journal of Geophysical Research: Solid Earth*, *120*, 7138–7155. https://doi.org/10.1002/2015JB012248

Maultzsch, S., Chapman, M., Liu, E., & Li, X. Y. (2003). Modelling frequency-dependent seismic anisotropy in fluid-saturated rock with aligned fractures: Implication of fracture size estimation from anisotropic measurements. *Geophysical Prospecting*, *51*(5), 381–392. https://doi.org/10.1046/j.1365-2478.2003.00386.x

Mavko, G., Mukerji, T., & Dvorkin, J. (2009). *The rock physics handbook: Tools for seismic analysis of porous media* (2nd ed.). Cambridge University Press. https://doi.org/10.1017/CBO9780511626753

Metz, B., Davidson, O., de Coninck, H., Loos, M., & Meyer, L. (2005). *IPCC special report on carbon dioxide capture and storage* (p. 431). Cambridge University Press.

Milani, M., Rubino, J. G., Müller, T. M., Quintal, B., Caspari, E., & Holliger, K. (2016). Representative elementary volumes for evaluating effective seismic properties of heterogeneous poroelastic media. *Geophysics*, *81*, D21–D181. https://doi.org/10.1190/GEO2015-0173.1

Montemagno, C., & Pyrak-Nolte, L. (1999). Fracture network versus single fractures: Measurement of fracture geometry with x-ray tomography. *Physics and Chemistry of the Earth, Part A: Solid Earth and Geodesy*, *24*(7), 575–579. https://doi.org/10.1016/S1464-1895(99)00082-4

Müller, T. M., Gurevich, B., & Lebedev, M. (2010). Seismic wave attenuation and dispersion resulting from wave-induced flow in porous rocks—A review. *Geophysics*, *75*, 75A147–75A164. https://doi.org/10.1190/1.3463417

Müller, T. M., & Rothert, E. (2006). Seismic attenuation due to wave-induced flow: Why Q in random structures scales differently. *Geophysical Research Letters*, *33*, L16305. https://doi.org/10.1029/2006GL026789

Nakagawa, S., Kneafsey, T. J., Daley, T. M., Freifeld, B. M., & Rees, E. V. (2013). Laboratory seismic monitoring of supercritical CO_2 flooding in sandstone cores using the split Hopkinson resonant bar technique with concurrent X-ray computed tomography imaging. *Geophysical Prospecting*, *61*(2), 254–269. https://doi.org/10.1111/1365-2478.12027

Nakagawa, S., Pride, S. R., & Nihei, K. T. (2019). Interaction of a normally-incident plane wave with a nonlinear poroelastic fracture. *The Journal of the Acoustical Society of America*, *146*(3), 1705–1720. https://doi.org/10.1121/1.5124691

Nakagawa, S., & Schoenberg, A. (2007). Poroelastic modeling of seismic boundary conditions across a fracture. *The Journal of the Acoustical Society of America*, *122*, 831–847. https://doi.org/10.1121/1.2747206

Pimienta, L., Fortin, J., & Guguen, Y. (2015). Bulk modulus dispersion and attenuation in sandstones. *Geophysics*, *80*(2), D111–D127. https://doi.org/10.1190/geo2014-0335.1

Pride, S. R. (2005). Relationships between seismic and hydrological properties. In Y. Rubin, & S. Hubbard (Eds.), *Hydrogeophysics* (pp. 253–290). Springer.

Pride, S. R., Berryman, J. G., & Harris, J. M. (2004). Seismic attenuation due to wave-induced flow. *Journal of Geophysical Research*, *109*, B01201. https://doi.org/10.1029/2003JB002639

Quintal, B., Caspari, E., Holliger, K., & Steeb, H. (2019). Numerically quantifying energy loss caused by squirt flow. *Geophysical Prospecting*, *67*(8), 2196–2212. https://doi.org/10.1111/1365-2478.12832

Quintal, B., Jänicke, R., Rubino, J. G., Steeb, H., & Holliger, K. (2014). Sensitivity of S-wave attenuation to the connectivity of fractures in fluid-saturated rocks. *Geophysics*, *79*(5), WB15–WB24. https://doi.org/10.1190/geo2013-0409.1

Quintal, B., Rubino, J. G., Caspari, E., & Holliger, K. (2016). A simple hydromechanical approach for simulating squirt-type flow. *Geophysics*, *81*(4), D335–D344. https://doi.org/10.1190/geo2015-0383.1

Quintal, B., Steeb, H., Frenher, M., & Schmalholz, S. M. (2011). Quasi-static finite element modeling of seismic attenuation and dispersion due to wave-induced fluid flow in poroelastic media. *Journal of Geophysical Research*, *116*, B01201. https://doi.org/10.1029/2010JB007475

Rubino, J. G., Caspari, E., Müller, T. M., & Holliger, K. (2017). Fracture connectivity can reduce the velocity anisotropy of seismic waves. *Geophysical Journal International*, *210*(1), 223–227. https://doi.org/10.1093/gji/ggx159

Rubino, J. G., Caspari, E., Müller, T. M., Milani, M., Barbosa, N. D., & Holliger, K. (2016). Numerical upscaling in 2-d heterogeneous poroelastic rocks: Anisotropic attenuation and dispersion of seismic waves. *Journal of Geophysical Research: Solid Earth*, *121*, 6698–6721. https://doi.org/10.1002/2016JB013165

Rubino, J. G., Guarracino, L., Müller, T. M., & Holliger, K. (2013). Do seismic waves sense fracture connectivity? *Geophysical Research Letters*, *40*, 692–696. https://doi.org/10.1002/grl.50127

Rubino, J. G., Müller, T. M., Milani, M., & Holliger, K. (2014). Seismic attenuation and velocity dispersion in fractured rocks: The role played by fracture contact areas. *Geophysical Prospecting*, *62*(6), 1278–1296. https://doi.org/10.1111/1365-2478.12170

Schoenberg, M. (1980). Elastic wave behavior across linear slip interfaces. *The Journal of the Acoustical Society of America*, *68*(5), 1516–1521. https://doi.org/10.1121/1.385077

Solazzi, S. G., Rubino, J. G., Müller, T. M., Milani, M., Guarracino, L., & Holliger, K. (2016). An energy-based approach to estimate seismic attenuation due to wave-induced fluid flow in heterogeneous poroelastic media. *Geophysical Journal International*, *207*(2), 823–832. https://doi.org/10.1093/gji/ggw302

Spencer, J. W., & Shine, J. (2016). Seismic attenuation and modulus dispersion in sandstones. *Geophysics*, *81*(3), D219–D231. https://doi.org/10.1190/GEO2015-0342.1

Subramaniyan, S., Quintal, B., Madonna, C., & Saenger, E. H. (2015). Laboratory-based seismic attenuation in Fontainebleau sandstone: Evidence of squirt flow. *Journal of Geophysical Research: Solid Earth*, *120*, 7526–7535. https://doi.org/10.1002/2015JB012290

Tester, J. W., Anderson, B. J., Batchelor, A. S., Blackwell, D. D., DiPippo, R., Drake, E. M., et al. (2007). Impact of enhanced geothermal systems on us energy supply in the twenty-first century. *Philosophical Transactions of the Royal Society A: Mathematical, Physical and Engineering Sciences*, *365*(1853), 1057–1094. https://doi.org/10.1098/rsta.2006.1964

Tillotson, P., Chapman, M., Sothcott, J., Best, A. I., & Li, X.-Y. (2014). Pore fluid viscosity effects on P- and S-wave anisotropy in synthetic silica-cemented sandstone with aligned fractures. *Geophysical Prospecting*, *62*(6), 1238–1252. https://doi.org/10.1111/1365-2478.12194

White, J. E., Mikhaylova, N. G., & Lyakhovitsky, F. M. (1975). Low-frequency seismic waves in fluid-saturated layered rocks. *Physics of the Solid Earth*, *11*, 654–S30. https://doi.org/10.1121/1.1995164